Viscoelasticity and viscoplasticity of polypropylene/polyethylene blends

A.D. Drozdov [a,*], J.deC. Christiansen [b], R. Klitkou [b], C.G. Potarniche [b]

[a] Danish Technological Institute, Gregersensvej 1, Taastrup 2630, Denmark
[b] Department of Production, Aalborg University, Fibigerstraede 16, Aalborg 9220, Denmark

ARTICLE INFO

ABSTRACT

Observations are reported on polypropylene/polyethylene blends with various concentrations of components in uniaxial tensile tests with constant strain rates, relaxation tests, and creep tests at room temperature. A model is developed for the viscoelastic and viscoplastic responses of polymer blends at arbitrary three-dimensional deformation with small strains. Material constants in the constitutive equations are determined by fitting the experimental data. It is found that all adjustable parameters evolve with blend composition following an analog of the rule of mixture. Lifetime of blends under condition of creep rupture is evaluated by numerical simulation.

© 2010 Elsevier Ltd. All rights reserved.

1. Introduction

This paper focuses on the experimental investigation and constitutive modeling of the viscoelastic and viscoplastic behavior of polymer blends. A binary blend of polypropylene (PP) and polyethylene (PE) is chosen for the analysis for the following reasons:

1. PP/PE blends are widely used in industry for production of ropes, nets, packaging materials, as well as for structural applications (Mathew et al., 2010; Zahran et al., 2010).
2. Analysis of the crystalline structure, thermal properties, and mechanical response of PP/PE blends have been a focus of attention in the past decade (Jose et al., 2004; Na et al., 2005; Xie et al., 2009).

A novelty of this study consists in the analysis of blends, where polypropylene is produced by metallocene catalysis (which ensures a narrow distribution of its molecular weight). Mechanical properties of PP/PE blends with metallocene catalysed PE were recently investigated by Li et al. (2003) and Razavi-Nouri (2007). Only Ono et al. (2009) studied the response of PP/PE blends with metallocene catalysed PP, but within a rather limited experimental program.

The objective of this work is fourfold:

1. To report observations on blends of metallocene catalysed PP and low density PE with various concentrations of components in tensile tests with various strain rates, relaxation tests, and creep tests.

2. To derive a constitutive model for the viscoelastic and viscoplastic behavior of binary polymer blends and to find adjustable parameters in the stress–strain relations by fitting the experimental data in tensile tests and relaxation tests.
3. To validate the constitutive equations by comparison of observations in creep tests with results of numerical simulation.
4. To apply the model for lifetime prediction under conditions of creep rupture.

To the best of our knowledge, no stress–strain relations have previously been suggested for the description of the viscoelastic and viscoplastic behavior of polymer blends with variable mass fractions of components. Constitutive models for the analysis of plastic deformations, damage and cavitation of polymers toughened with rubber particles were proposed by Steenbrink and van der Giessen (1997), Chen and Mai (1999), Liang and Li (2000), Kuroda et al. (2004), and Mae et al. (2008). Thermo-viscoelasticity of polymer blends was recently modeled by Machmud et al. (2006) and Shaoqiu et al. (2007). The viscoelasto-plastic behavior of a polymer blend reinforced with nanoclay was analyzed by Drozdov and Christiansen (2007) for a fixed composition of the matrix. The aim of this study is to derive constitutive equations for the time- and rate-dependent response of polymer blends that involve a small number of adjustable parameters which change consistently with composition following an analog of the rule of mixture.

The exposition is organized as follows. Observations in mechanical tests are presented in Section 2. A constitutive model is developed in Section 3 for arbitrary three-dimensional deformations with small strains. Adjustable parameters in the stress–strain relations are determined in Section 4 by matching the experimental data. Results of numerical simulation for long-term creep tests

---

* Corresponding author. Tel.: +45 72 20 31 42; fax: +45 72 20 31 12.
E-mail address: Aleksey.Drozdov@teknologisk.dk (A.D. Drozdov).

are reported in Section 5. Concluding remarks are formulated in Section 6.

2. Experimental results

2.1. Preparation of polymer blends

As components of a binary blend, low density polyethylene (LDPE) and metallocene catalysed polypropylene (mPP) are chosen. Low density polyethylene Riblene FL 20 (density 0.921 g/cm^3, melt flow rate 2.2 g/10 min [190 °C, 2.16 kg], melting temperature 109 °C) was supplied by Polimeri Europa (Italy). Metallocene catalysed polypropylene homopolymer Metocene HM 562S (density 0.98 g/cm^3, melt flow rate 30 g/10 min [230 °C, 2.16 kg], melting temperature 145 °C) was purchased from Lyondell Basell Ind. (Switzerland).

Pellets of LDPE and mPP were carefully mixed at required proportions and dried. The blends were melt mixed by using thermoscientific twin screw extruder Prism Eurolab 16 and pelletized. The extrusion process was conducted with the processing temperature T = 200°C, screw speed 200 rpm, and throughput 1 kg/h. It was repeated twice to obtain homogeneous distribution of components. Six blends were prepared with different proportions of LDPE and mPP. These blends are characterized by mass fraction of mPP k with k = 0.0, 0.2, 0.4, 0.6, 0.8, and 1.0.

Dumbbell specimens for tensile tests (ASTM standard D–638) with cross-sectional area 9.9 mm × 3.9 mm were molded by using injection-molding machine Ferromatic K110/S60–2 K.

2.2. Mechanical tests

Mechanical tests were performed at room temperature by means of a universal testing machine Instron–5568 equipped with two electro-mechanical sensors for measurements of longitudinal (Instron Static 2630–113) and transverse (Epsilon 3574–250M) strains. Tensile force was measured by a 50 kN load cell. The engineering stress σ was determined as the ratio of axial force to cross-sectional area of specimens in the stress-free state. The experimental program involved three series of tests. Each test was conducted on a virgin specimen and repeated by twice.

2.2.1. Stretching with constant strain rates

The first series consisted on tensile tests with cross-head speeds $\dot{d} = 1, 10$, and 100 mm/min (which corresponded to strain rates $\dot{\epsilon} = 2.3 \cdot 10^{-4}, \dot{\epsilon} = 2.3 \cdot 10^{-3}$, and $\dot{\epsilon} = 2.3 \cdot 10^{-2}$ s^{-1}, respectively) and maximum tensile strain ϵ_{max} = 0.25.

Experimental data in tensile tests are depicted in Figs. 1–3, where engineering stress σ is plotted versus strain ϵ. These figures reveal a strong nonlinearity of the stress–strain diagrams. At low concentrations k of mPP, the stress–strain dependencies $\sigma(\epsilon)$ are monotonic. When k exceeds 0.2, they become non-monotonic with pronounced yield points.

Figs. 1–3 show that for any strain ϵ, stress σ monotonically grows with mass fraction of mPP k and strain rate $\dot{\epsilon}$. To rationalize the latter dependence, yield stress σ_y is determined for each stress–strain curve with $k \geqslant 0.4$ as the point of maximum on an appropriate diagram. This parameter is plotted versus strain rate $\dot{\epsilon}$ in Fig. 4. The data are approximated by the Eyring equation (Bauwens-Crowet et al., 1972)

$$\sigma_y = \sigma_{y0} + \sigma_{y1} \log \dot{\epsilon}, \tag{1}$$

with log = $\log_{10}$. The coefficients σ_{y0} and σ_{y1} in Eq. (1) are calculated by the least-squares method. Fig. 4 demonstrates that Eq. (1) correctly approximates the observations.
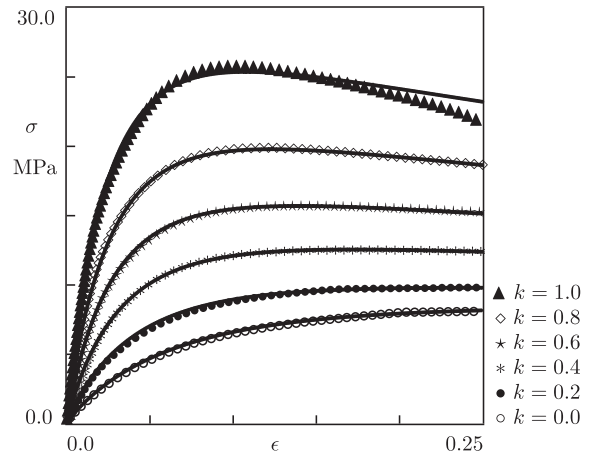

Fig. 1. Stress σ versus strain ϵ. Symbols: experimental data in tensile tests with cross-head speed 1 mm/min on blends with various concentrations k of mPP. Solid lines: results of numerical simulation.

Fig. 2. Stress σ versus strain ϵ. Symbols: experimental data in tensile tests with cross-head speed 10 mm/min on blends with various concentrations k of mPP. Solid lines: results of numerical simulation.
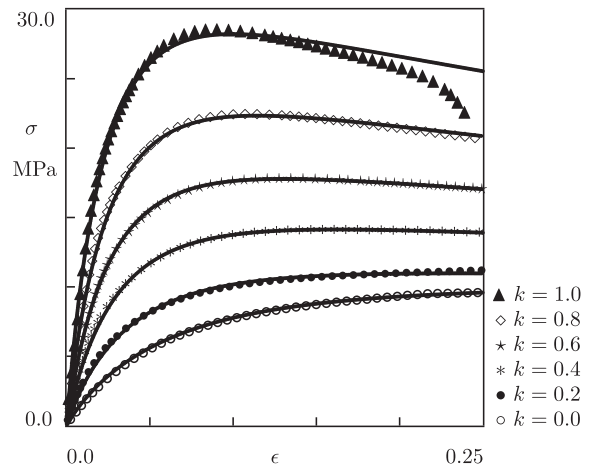

Fig. 3. Stress σ versus strain ϵ. Symbols: experimental data in tensile tests with cross-head speed 100 mm/min on blends with various concentrations k of mPP. Solid lines: results of numerical simulation.
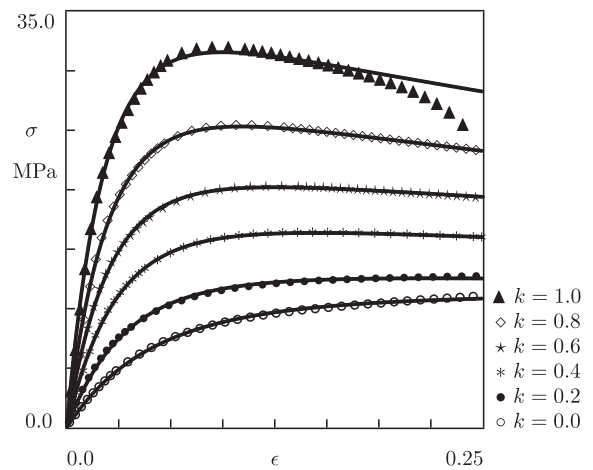
To assess compressibility of PP/PE blends, transverse strain ϵ_t is plotted versus tensile strain ϵ, and the experimental data are approximated by the linear equation
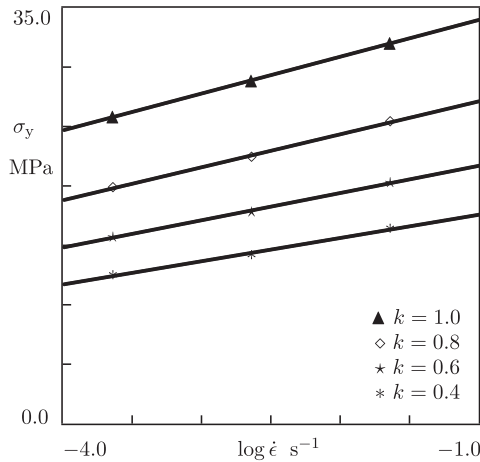
Fig. 4. Yield stress σ_y versus strain rate $\dot\epsilon$. Symbols: treatment of observations in tensile tests on blends with various concentrations k of mPP. Solid lines: approximation of the experimental data by Eq. (1).

Fig. 6. Stress σ versus relaxation time t'. Symbols: experimental data in relaxation tests with $\epsilon = 0.02$ on blends with various concentrations k of mPP. Solid lines: results of numerical simulation.

$$\epsilon_t = -\nu\epsilon, \tag{2}$$

where Poisson's ratio ν is calculated by the least-squares technique. Some observations (for neat LDPE and mPP) are reported in Fig. 5. This figure demonstrates that (i) Eq. (2) correctly fits the experimental curves below appropriate yield points, and (ii) Poisson's ratios of blends are close to $\nu = 0.5$, the value characteristic for incompressible media. Deviations of the experimental data from their approximations by Eq. (2) in the post-yield region of deformations are attributed to an increase in volume strain induced by nucleation, growth, and coalescence of micro-voids.

2.2.2. Relaxation tests

The other series involved tensile relaxation tests with strain $\epsilon = 0.02$. In each test, a specimen was loaded with a constant cross-head speed 100 mm/min up to the required strain. Afterwards, a decrease in tensile stress was monitored a function of time while the strain was preserved constant. Following the protocol ASTM E–328 for short-term relaxation tests, the duration of relaxation test $t_{rel} = 20$ min was chosen.

Experimental data in relaxation tests are reported in Fig. 6. Following common practice, semi-logarithmic plots are employed, where stress σ is depicted versus logarithm of relaxation time
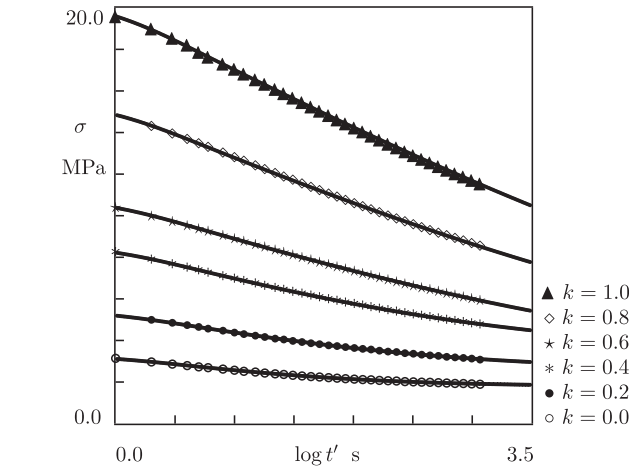
$t' = t - t_0$ (t_0 stands for the instant when relaxation starts). Fig. 6 demonstrates that the growth of mass fraction of mPP k results in a strong increase in stress σ and noticeable changes in the shape of relaxation curves.

2.2.3. Creep tests

The third series consisted of two kinds of tensile creep tests. In creep tests of the first kind, specimens were stretched with a constant cross-head speed 100 mm/min up to stress $\sigma = 5$ MPa. Afterwards, an increase in strain was monitored a function of time while the stress was preserved constant. In creep tests of the second kind, stretching was performed until the tensile strain reached a fixed value $\epsilon = 0.03$. Then the stress was fixed, and tensile strain was measured as a function of time. Following the protocol ASTM D–2990 for short-term creep tests, the duration of creep tests $t_{cr} = 20$ min was chosen.

Experimental data tests are reported in Figs. 7–9, where strain ϵ is plotted versus time t. Fig. 7 presents observations in creep tests with $\sigma = 5$ MPa. Observations in tests where creep flow starts at strain $\epsilon = 0.03$ are depicted in Figs. 8 and 9. Creep curves measured at relatively small and large stresses σ are reported in two figures to avoid overlapping of data.
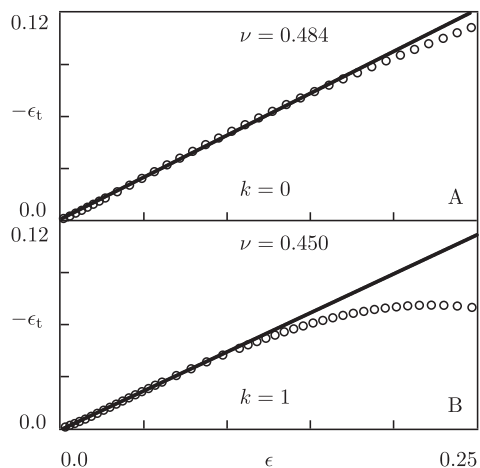

Fig. 5. Transverse strain ϵ_t versus tensile strain ϵ. Circles: experimental data in tensile tests with cross-head speed 100 mm/min on LDPE (A) and mPP (B). Solid lines: approximation of the experimental data by Eq. (2).
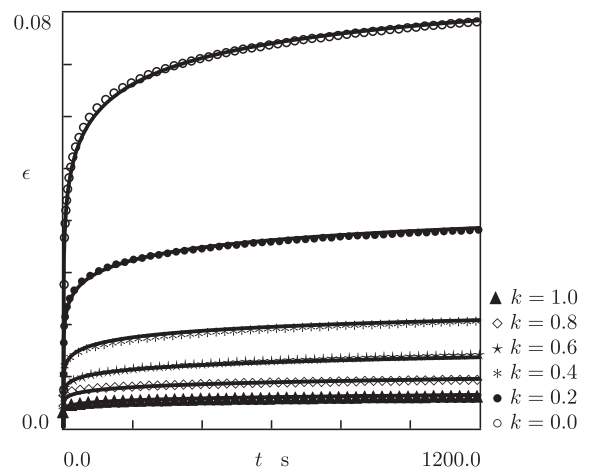

Fig. 7. Strain ϵ versus time t. Symbols: experimental data in creep tests with stress $\sigma = 5$ MPa on blends with various concentrations k of mPP. Solid lines: predictions of the model.
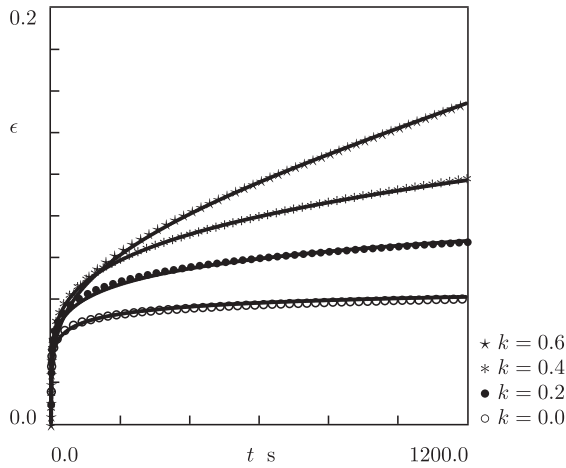
Fig. 8. Strain ϵ versus time t. Symbols: experimental data in creep tests with the initial strain $\epsilon_0 = 0.03$ on blends with various concentrations k of mPP (○ $\sigma = 4.4$; ● $\sigma = 7.3$; * $\sigma = 11.1$; ★ $\sigma = 14.9$ MPa). Solid lines: predictions of the model.
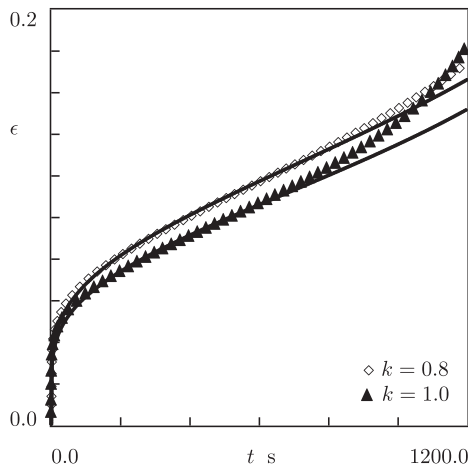

Fig. 9. Strain ϵ versus time t. Symbols: experimental data in creep tests with the initial strain $\epsilon_0 = 0.03$ on blends with various concentrations k of mPP (◇ $\sigma = 18.7$; ▲ $\sigma = 23.7$ MPa). Solid lines: predictions of the model.

Figs. 7–9 reveal that the time-dependent response of blends is rather sophisticated. Two characteristic features of the observations are mentioned: (i) intersection of creep curves at stresses σ exceeding 15 MPa, and (ii) transition from secondary to tertiary creep observed in tests with relatively large stresses.

2.2.4. Accuracy of measurements

Experimental data demonstrate good reproducibility of measurements. In tensile tests with constants strain rates, the maximum deviation between stresses measured on different specimens with the same composition does not exceed 2%, and that for transverse strains is less than 3%. In relaxation tests, deviations between stresses measured on different samples are less than 1.5%. In creep tests, deviations between strains measured on different samples do not exceed 2% at relatively small stresses (Figs. 7 and 8) and 6% at large stresses (Fig. 9).

3. Constitutive model

To rationalize the effect of composition of polymer blends on their mechanical behavior, a constitutive model is developed for the viscoelastic and viscoplastic responses at arbitrary three-dimensional deformations with small strains. Constitutive equations for a binary blend are derived by using the Clausius–Duhem inequality.

To develop stress–strain relations that involve a relatively small number of material constants, a homogenization concept is applied (Drozdov and Christiansen, 2008). A binary blend of semicrystalline polymers with a complicated micro-structure is modeled as an equivalent one-phase continuum whose mechanical behavior coincides with that of the blend. An incompressible, heterogeneous, transient, non-affine network of chains is chosen as the equivalent medium. For the sake of simplicity, damage accumulation in blends of semicrystalline polymers observed as growth of micro-voids in the post-yield region of deformations (Fig. 5) is not accounted for by the model.

Two types of chains are distinguished in an equivalent network: permanent and temporary (Tanaka and Edwards, 1992). Denote by N_1 and N_2 the numbers of permanent and active temporary chains per unit volume, respectively. Permanent chains do not detach from their junctions, whereas temporary chains are rearranged. When an end of an active temporary chain separates from its junction at some instant τ_1, the chain is transformed into the dangling state. When the free end of a dangling chain merges with the network at instant $\tau_2 > \tau_1$, the chain returns into the active state. Attachment and detachment of temporary chains occur at random times being driven by thermal fluctuations.

An inhomogeneous equivalent network consists of meso-regions with various activation energies for rearrangement of chains. In the stress-free state, the rate of separation of active chains from their junctions in a meso-domain with activation energy u is governed by the Eyring equation

$$\Gamma = \gamma \exp\left(-\frac{u}{k_B T}\right),$$

where γ stands for an attempt rate, T is the absolute temperature, and k_B denotes Boltzmann's constant. Confining ourselves to isothermal processes at a fixed temperature T and introducing the dimensionless energy $v = u/(k_B T)$, we present this relation in the form

$$\Gamma(v) = \gamma \exp(-v), \tag{3}$$

where the pre-factor γ is assumed to be independent of mechanical factors.

Non-affinity of the equivalent network means that junctions between chains slide with respect to their reference positions under deformation. Sliding (plastic flow) of junctions is described by the strain tensor $\hat{\epsilon}_p$. The latter is presented as the sum of two components

$$\hat{\epsilon}_p = \hat{\epsilon}_{p1} + \hat{\epsilon}_{p2}, \tag{4}$$

that characterize inelastic deformations of the amorphous matrix and crystallites. Irreversible deformations in the crystalline phase reflect (i) inter-lamellar separation, (ii) rotation and twist of lamellae, (iii) fine (homogeneous shear of layer-like crystalline structures) and coarse (heterogeneous inter-lamellar sliding) slip of lamellar blocks (Machado et al., 2009). Inelastic deformations in the amorphous phase describe (i) chain slip through the crystals, (ii) sliding of tie chains along and their detachment from lamellar blocks, and (iii) detachment of chain folds and loops from surfaces of crystal blocks (Hiss et al., 1999). The difference between tensors $\hat{\epsilon}_{p1}$ and $\hat{\epsilon}_{p2}$ is that their evolution is driven by different factors. The rate-of-strain tensor $d\hat{\epsilon}_{p1}/dt$ is proportional to the rate-of-strain tensor for macro-deformation $d\hat{\epsilon}/dt$, and the rate-of-strain tensor $d\hat{\epsilon}_{p2}/dt$ is proportional to the deviatoric component $\hat{\sigma}'$ of the stress tensor $\hat{\sigma}$

$$\frac{d\hat{\epsilon}_{p1}}{dt} = \phi \frac{d\hat{\epsilon}}{dt}, \quad \frac{d\hat{\epsilon}_{p2}}{dt} = \psi \hat{\sigma}', \tag{5}$$

where $0 \leqslant \phi(t) \leqslant 1$ and $\psi(t) \geqslant 0$ are function to be defined in what follows. To explain the physical meaning of Eq. (5), it is convenient to consider sliding processes in amorphous and crystalline domains separately. When $\hat{\epsilon}_{p2} = 0$ (no slip in crystalline lamellae), the first equality in Eq. (5) presents a simple version of a model for kinetic friction that describes a delay in sliding of junctions between chains in a non-affine network due to stick–slip events with respect to macro-deformation ($\phi = 0$ for an affine network). When $\hat{\epsilon}_{p1} = 0$ (no sliding in amorphous regions), the last equality in Eq. (5) expresses the simplest law of plastic flow, which states that the rate of plastic deformation is proportional to an appropriate stress.

3.1. Rearrangement of a transient network

Rearrangement of a transient network is described by the function $n(t, \tau, v)$ that equals the number (per unit volume) of temporary chains at time $t \geqslant 0$ that has returned into the active state before instant $\tau \leqslant t$ and belong to a meso-domain with activation energy v. In particular, the number of temporary chains in meso-domains with activation energy v at time t reads $n(t, t, v)$, and the number of temporary chains that were active in the reference state and have not separated from their junctions until time t is given by $n(t, 0, v)$. The number of temporary chains that were active at the initial instant and detach from their junctions within the interval $[t, t + dt]$ reads $-\partial n/\partial t(t, 0, v)\,dt$, the number of dangling chains that return into the active state within the interval $[\tau, \tau + d\tau]$ is given by $P(\tau, v)\,d\tau$ with

$$P(\tau, v) = \left.\frac{\partial n}{\partial \tau}(t, \tau, v)\right|_{t=\tau}, \tag{6}$$

and the number of chains (per unit volume) that merged (for the last time) with the network within the interval $[\tau, \tau + d\tau]$ and detach from their junctions within the interval $[t, t + dt]$ equals $-\partial^2 n/\partial t \partial \tau(t, \tau, v)\,dt\,d\tau$.

The number of active temporary chains (per unit volume) in meso-domains with activation energy v at time t is presented in the form

$$n(t, t, v) = N_2 f(v), \tag{7}$$

where $f(v)$ stands for the distribution function of meso-regions with various activation energies.

Detachment of active chains from their junctions is described by the kinetic equations

$$\frac{\partial n}{\partial t}(t, 0, v) = -\Gamma(v)n(t, 0, v), \quad \frac{\partial^2 n}{\partial t \partial \tau}(t, \tau, v) = -\Gamma(v)\frac{\partial n}{\partial \tau}(t, \tau, v), \tag{8}$$

which state that the rate of transformation of active chains into the dangling state is proportional to the number of active chains in an appropriate meso-region. Integration of Eq. (8) with initial conditions (6) and (7) implies that

$$n(t, 0, v) = N_2 f(v) \exp[-\Gamma(v)t],$$
$$\frac{\partial n}{\partial \tau}(t, \tau, v) = N_2 \Gamma(v) f(v) \exp[-\Gamma(v)(t - \tau)]. \tag{9}$$

3.2. Stress–strain relations

At small strains, the strain tensor for elastic deformation $\hat{\epsilon}_e$ is given by

$$\hat{\epsilon}_e = \hat{\epsilon} - \hat{\epsilon}_p, \tag{10}$$

where $\hat{\epsilon}$ stands for the strain tensor for macro-deformation. The strain energy of a chain is determined by the formula

$w = \frac{1}{2}\bar{\mu}\hat{\epsilon}_e : \hat{\epsilon}_e$, where $\bar{\mu}$ stands for rigidity of a chain, and colon denotes convolution. Under the assumption that the energy of inter-chain interaction is accounted for by the incompressibility condition, the strain energy density per unit volume of the network is calculated as the sum of strain energies of active chains

$$W(t) = \frac{1}{2}\bar{\mu}\left[N_1 \hat{\epsilon}_e(t) : \hat{\epsilon}_e(t) + \int_0^\infty n(t, 0, v)\,dv\hat{\epsilon}_e(t) : \hat{\epsilon}_e(t) \right.$$
$$\left. + \int_0^\infty dv \int_0^t \frac{\partial n}{\partial \tau}(t, \tau, v)\big(\hat{\epsilon}_e(t) - \hat{\epsilon}_e(\tau)\big) : \big(\hat{\epsilon}_e(t) - \hat{\epsilon}_e(\tau)\big)d\tau\right]. \tag{11}$$

The first term in Eq. (11) equals the strain energy of permanent chains, the other term equals the strain energy of temporary chains that have not been rearranged within the interval $[0, t]$, and the last term expresses the strain energy of chains that have last merged with the network at various instants $\tau \in [0, t]$. It is presumed that stresses totally relax in dangling chains before they merge with the network, which implies that the strain energy (at time t) of a chain transformed into the active state at time τ depends on the relative elastic strain tensor $\hat{\epsilon}_e^*(t, \tau) = \hat{\epsilon}_e(t) - \hat{\epsilon}_e(\tau)$.

For isothermal deformation of an incompressible medium, the Clausius–Duhem inequality reads

$$Q = -\frac{dW}{dt} + \hat{\sigma}' : \frac{d\hat{\epsilon}}{dt} \geqslant 0, \tag{12}$$

where Q stands for internal dissipation per unit volume and unit time. Inserting Eq. (11) into Eq. (12) and using Eqs. (4), (5), (8), and (10), we find that the second law of thermodynamics is satisfied for an arbitrary deformation process, provided that the stress tensor reads

$$\hat{\sigma}(t) = -p(t)\hat{I} + \mu(1 - \phi(t))$$
$$\times \left[\hat{\epsilon}_e(t) - \kappa \int_0^\infty \Gamma(v)f(v)dv \int_0^t \exp(-\Gamma(v)(t - \tau))\hat{\epsilon}_e(\tau)d\tau\right], \tag{13}$$

where p stands for an unknown pressure, $\hat{I}$ denotes the unit tensor, $\mu = \bar{\mu}(N_1 + N_2)$, and $\kappa = N_2/(N_1 + N_2)$. The rate of internal dissipation reads

$$Q(t) = \frac{\psi(t)}{1 - \phi(t)}\hat{\sigma}'(t) : \hat{\sigma}'(t)$$
$$+ \frac{1}{2}\bar{\mu}\left[\int_0^\infty \Gamma(v)n(t, 0, v)dv\hat{\epsilon}_e(t) : \hat{\epsilon}_e(t)\right.$$
$$\left. + \int_0^\infty \Gamma(v)dv \int_0^t \frac{\partial n}{\partial \tau}(t, \tau, v)\big(\hat{\epsilon}_e(t) - \hat{\epsilon}_e(\tau)\big) : \big(\hat{\epsilon}_e(t) - \hat{\epsilon}_e(\tau)\big)d\tau\right] \geqslant 0.$$

3.3. Material functions and adjustable parameters

The stress–strain relation (13) together with kinematic Eqs. (4), (5), (10), and formula (3) for the rate of rearrangement of active chains involve three material functions $f(v)$, $\phi(t)$, and $\psi(t)$.

With reference to the random energy model (Derrida, 1980), the quasi-Gaussian formula is adopted for the distribution function f

$$f(v) = f_0 \exp\left(-\frac{v^2}{2\Sigma^2}\right) \quad (v \geqslant 0), \quad f(v) = 0 \quad (v < 0). \tag{14}$$

An advantage of Eq. (14) is that it is characterized by the only parameter $\Sigma > 0$. The pre-factor f_0 is determined from the normalization condition $\int_0^\infty f(v)dv = 1$.

The coefficient of proportionality ϕ between the rate of sliding of junctions in the amorphous phase and the rate of macro-deformation obeys the conditions: (i) ϕ equals zero in the reference state (which means that junctions do not slide at very small deformations), (ii) it monotonically increases with strain (which reflects

acceleration of plastic flow under loading), and (iii) it tends to the ultimate value $\phi(\infty) = 1$ at relatively large deformations (which implies that the rate of developed plastic flow coincides with that of macro-deformation). To fulfil these requirements, evolution of ϕ with time is presumed to be governed by the differential equation

$$\frac{\mathrm{d}\phi}{\mathrm{d}t} = a(1 - \phi)^2 \dot{\epsilon}_{eq}, \tag{15}$$

where a is a dimensionless positive coefficient, and

$$\dot{\epsilon}_{eq} = \left(\frac{2}{3} \frac{\mathrm{d}\hat{\epsilon}}{\mathrm{d}t} : \frac{\mathrm{d}\hat{\epsilon}}{\mathrm{d}t} \right)^{\frac{1}{2}}$$

stands for the equivalent strain rate for macro-deformation. Eq. (15) is a conventional kinetic equation of the second order. To justify this order, one can speculate that sliding of junctions in the amorphous phase accelerates slippage of crystalline lamellae, which, in turn, results in the growth of rate of plastic flow in amorphous regions.

The coefficient ψ in Eq. (5) is presented in the form

$$\psi = \frac{b}{\mu} \dot{\epsilon}_{eq}. \tag{16}$$

The dimensionless rate of plastic flow in crystallites b obeys the equation similar to Eq. (1)

$$b = b_0 + b_1 \log \dot{\epsilon}_{eq}, \tag{17}$$

where b_0 and b_1 are material parameters.

The viscoelastic and viscoplastic behavior of a polymer blend with a given composition is described by the constitutive Eq. (13) that involves seven material constants, μ, a, b_0, b_1, γ, κ, and Σ, with transparent physical meaning:

1. μ stands for shear modulus of an equivalent network,
2. κ characterizes concentration of temporary chains,
3. Σ is a measure of heterogeneity of the equivalent network,
4. γ denotes rate of detachment of chains from their junctions,
5. a stands for rate of plastic flow in the amorphous phase,
6. b_0 and b_1 characterize rates of fine and coarse slip of lamellar blocks.

To account for the effect of blend composition on adjustable parameters in the stress–strain relations, we presume γ and b_1 to be independent of k and introduce the following phenomenological equations:

$$\mu = \mu_0 + \mu_1 k, \quad \kappa = \kappa_0 + \kappa_1 k, \quad \Sigma = \Sigma_0 + \Sigma_1 k,$$
$$a = a_1 k, \quad b_0 = B_0 + B_1 k. \tag{18}$$

4. Fitting of observations

To find adjustable parameters in the constitutive equations, the experimental data depicted in Figs. 1–3 and 6 are fitted.

4.1. Uniaxial tension

We begin with simplification of the stress–strain relations for uniaxial tension of an incompressible specimen. Under stretching along the x_1 axis of a Cartesian coordinate frame $\{x_1, x_2, x_3\}$, the strain tensors $\hat{\epsilon}$ and $\hat{\epsilon}_e$ read

$$\hat{\epsilon} = \epsilon \left[\mathbf{e}_1 \mathbf{e}_1 - \frac{1}{2} (\mathbf{e}_2 \mathbf{e}_2 + \mathbf{e}_3 \mathbf{e}_3) \right], \quad \hat{\epsilon}_e = \epsilon_e \left[\mathbf{e}_1 \mathbf{e}_1 - \frac{1}{2} (\mathbf{e}_2 \mathbf{e}_2 + \mathbf{e}_3 \mathbf{e}_3) \right], \tag{19}$$

where ϵ denotes tensile strain, ϵ_e is a function to be found, and $\mathbf{e}_i (i = 1, 2, 3)$ stand for unit vectors.

Inserting Eq. (19) into Eq. (13) and using the boundary conditions at the lateral surface of a specimen, we find that $\hat{\sigma} = \sigma \mathbf{e}_1 \mathbf{e}_1$ with

$$\sigma(t) = E(1 - \phi(t))$$
$$\times \left[\epsilon_e(t) - \kappa \int_0^\infty \Gamma(v) f(v) \mathrm{d}v \int_0^t \exp(-\Gamma(v)(t - \tau)) \epsilon_e(\tau) \mathrm{d}\tau \right], \tag{20}$$

where $E = \frac{3}{2} \mu$ stands for the Young's modulus. It follows from Eqs. (4) and (10) that

$$\epsilon_e(t) = \epsilon(t) - \epsilon_{p1}(t) - \epsilon_{p2}(t), \tag{21}$$

where the functions ϵ_{p1} and ϵ_{p2} are governed by the differential Eqs. (5), (15), and (16)

$$\frac{\mathrm{d}\epsilon_{p1}}{\mathrm{d}t} = \phi \frac{\mathrm{d}\epsilon}{\mathrm{d}t}, \quad \frac{\mathrm{d}\epsilon_{p2}}{\mathrm{d}t} = \frac{b\sigma}{E} \frac{\mathrm{d}\epsilon}{\mathrm{d}t}, \quad \frac{\mathrm{d}\phi}{\mathrm{d}t} = a(1 - \phi)^2 \frac{\mathrm{d}\epsilon}{\mathrm{d}t}. \tag{22}$$

4.2. Relaxation tests

For tensile relaxation test with a fixed strain ϵ, Eqs. (21) and (22) imply that ϵ_e and ϕ are constants. This assertion together with Eq. (20) results in

$$\sigma(t) = s_0 + s_1 \int_0^\infty f(v) \exp(-\Gamma(v)t) \mathrm{d}v, \tag{23}$$

where $\Gamma(v)$ is given by Eq. (3), and

$$s_0 = (1 - \kappa)\sigma_0, \quad s_1 = \kappa\sigma_0, \quad \sigma_0 = E(1 - \phi)\epsilon_e. \tag{24}$$

Adjustable parameters γ, κ, and Σ are determined by matching the observations reported in Fig. 6 with the help of the following algorithm. First, the experimental data on mPP ($k = 1$) are approximated. For this purpose, some intervals $[0, \gamma^\circ]$ and $[0, \Sigma^\circ]$ are fixed, where parameters γ and Σ are located. These intervals are divided into $J = 10$ sub-intervals by the points $\gamma^{(i)} = i\Delta\gamma$, $\Sigma^{(j)} = j\Delta\Sigma$ with $\Delta\gamma = \gamma^\circ/J$, $\Delta\Sigma = \Sigma^\circ/J (i, j = 0, 1, \ldots, J - 1)$. For each pair $\{\gamma^{(i)}, \Sigma^{(j)}\}$, the stress $\sigma(t)$ is found from Eq. (23), where the integral is calculated by the Simpson method with $v = n\Delta v$, $\Delta v = 0.2$, and $n = 0, 1, \ldots,$ 200. The coefficients s_0 and s_1 are determined by the least-squares technique from the condition of minimum of the function $F = \sum_m [\sigma^{exp}(t_m) - \sigma^{num}(t_m)]^2$, where summation is performed over all instants t_m at which observations are reported, σ^{exp} is the stress measured in an appropriate test, and σ^{num} is given by Eq. (23). The quantities γ and Σ are found from the condition of minimum of the function F. Then the initial intervals are replaced with the new intervals $[\gamma - \Delta\gamma, \gamma + \Delta\gamma]$ and $[\Sigma - \Delta\Sigma, \Sigma + \Delta\Sigma]$, and the calculations are repeated.

Afterwards, we fix the rate of rearrangement $\gamma = 0.89$ s^{-1} and approximate relaxation curves for blends with other concentrations of mPP by the above algorithm with the only adjustable parameter Σ. Each set of observations is fitted separately. Fig. 6 demonstrates good agreement between the experimental data and the results of numerical simulation.

For each composition of blends k, the coefficient κ is calculated from Eq. (24). The dependencies $\Sigma(k)$ and $\kappa(k)$ are depicted in Figs. 10 and 11 together with their approximations by Eq. (18), where the coefficients are determined by the least-squares technique. These figures show that Eq. (18) correctly fits the data.

4.3. Tensile tests with constant strain rates

To model tensile deformation with a constant strain rate $\dot{\epsilon}$, we present Eq. (20) in the form
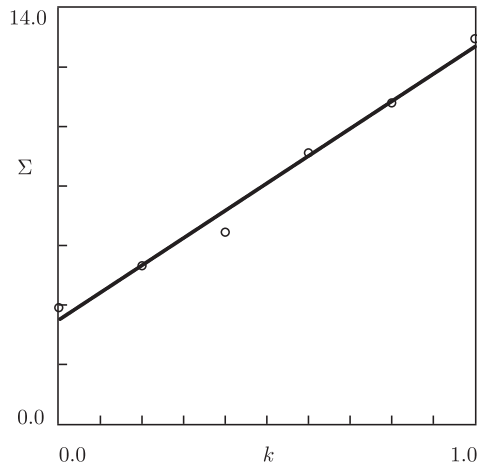
Fig. 10. Parameter Σ versus mass fraction of mPP k. Circles: treatment of observations in relaxation tests. Solid line: approximation of the experimental data by Eq. (18).
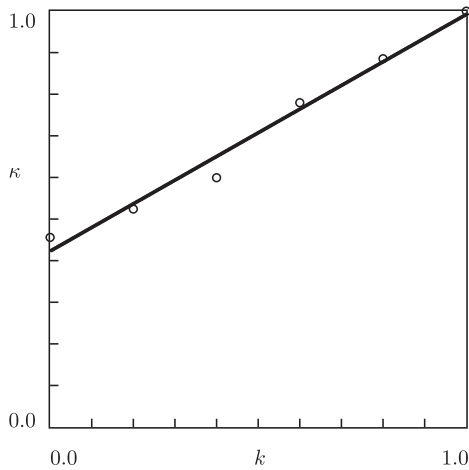

Fig. 11. Parameter κ versus mass fraction of mPP k. Circles: treatment of observations in relaxation tests. Solid line: approximation of the experimental data by Eq. (18).

$$\sigma(t) = E(1 - \phi(t)) \left[\epsilon_e(t) - \kappa \int_0^\infty f(v) Z(t, v) dv \right], \qquad (25)$$

where the function

$$Z(t, v) = \int_0^t \Gamma(v) \exp[-\Gamma(v)(t - \tau)] \epsilon_e(\tau) d\tau$$

obeys the differential equation

$$\frac{\partial Z}{\partial t}(t, v) = \Gamma(v)[\epsilon_e(t) - Z(t, v)], \quad Z(0, v) = 0. \qquad (26)$$

Adjustable parameters E, a, and b in Eqs. (22), (25), and (26) are found by matching the observations reported in Figs. 1–3. Each set of experimental data is approximated separately by means of the following algorithm.

We begin with matching observations on binary blends in tensile tests with cross-head speed 100 mm/min. For each stress–strain curve depicted in Fig. 3, some intervals $[0, a^\circ]$ and $[0, b^\circ]$ are fixed, where parameters a and b are located. Each of these intervals is divided into $J = 10$ sub-intervals by the points $a^{(i)} = i\Delta a$, $b^{(j)} = j\Delta b$ with $\Delta a = a^\circ/J$, $\Delta b = b^\circ/J$ ($i, j = 0, 1, \ldots, J - 1$). For each pair $\{a^{(i)}, b^{(j)}\}$, Eqs. (22), (25), and (26) are integrated the Runge–Kutta

method from $\epsilon = 0$ to $\epsilon = \epsilon_{max}$ with the time step $\Delta t = 5.0 \times 10^{-3}$ s. The integral in Eq. (25) is evaluated by the Simpson method with $v = n\Delta v$, $\Delta v = 0.2$, and $n = 0, 1, \ldots, 200$. The Young's modulus E is calculated by the least-squares technique from the condition of minimum of the function $F = \sum_m [\sigma^{exp}(\epsilon_m) - \sigma^{num}(\epsilon_m)]^2$, where summation is performed over strains ϵ_m at which the observations are reported, σ^{exp} is the engineering stress measured in the test, and σ^{num} is given by Eq. (25). After finding the best-fit parameters a and b from the condition of minimum of F, the initial intervals are replaced with the new intervals $[a - \Delta a, a + \Delta a]$, $[b - \Delta b, b + \Delta b]$, and the calculations are repeated.

Young's modulus E is presented as a function of mass fraction of mPP k in Fig. 12. The data are approximated by Eq. (18)

$$E = E_0 + E_1 k, \qquad (27)$$

where the coefficients are determined by the least-squares method. Fig. 12 demonstrates an acceptable agreement between the data and their prediction by Eq. (27), which means that the rule of mixture is fulfilled with high accuracy. Young's modulus E increases with k from 0.13 GPa (a typical value for LDPE) to 1.46 GPa (the modulus of mPP provided by the supplier).

The dimensionless parameter a is plotted versus mass fraction of mPP k in Fig. 13. The data are approximated by Eq. (18), where the coefficient a_1 is found by the least-squares method. Fig. 13
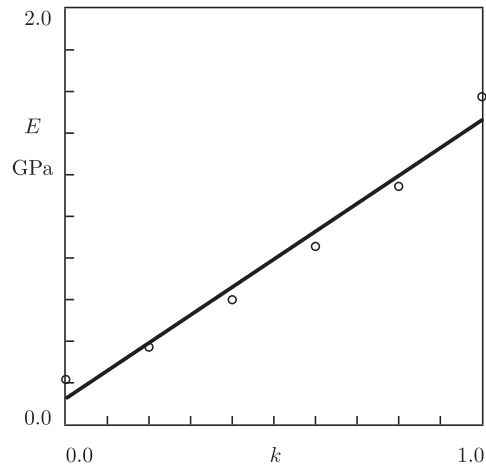

Fig. 12. Young's modulus E versus mass fraction of mPP k. Circles: treatment of observations. Solid line: approximation of the experimental data by Eq. (27).
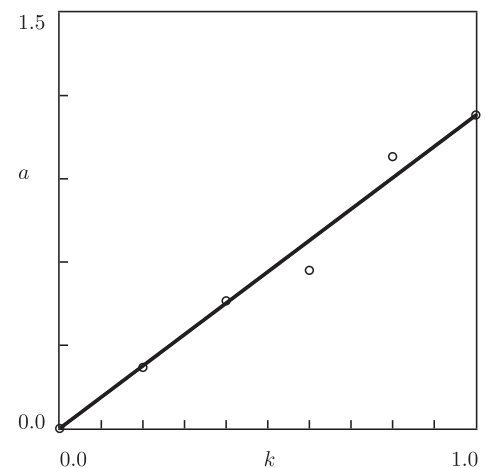

Fig. 13. Parameter a versus mass fraction of mPP k. Circles: treatment of observations. Solid line: approximation of the experimental data by Eq. (18).
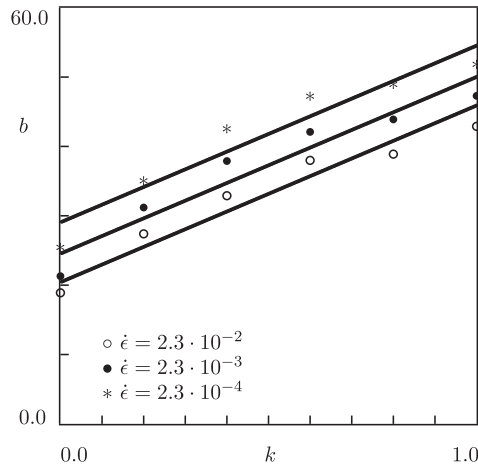
Fig. 14. Parameter b versus mass fraction of mPP k. Symbols: treatment of observations in tensile tests with various strain rates $\dot{\epsilon}$ s^{-1}. Solid lines: approximation of the experimental data by Eq. (28).

shows good agreement between the experimental dependence $a(k)$ and its fit by Eq. (18).

Afterwards, the functions $E(k)$ and $a(k)$ are fixed, and observations in tensile tests with cross-head speeds 1 and 10 mm/min are matched by using the above algorithm with the only adjustable parameter b.

The dimensionless parameter b is plotted versus k in Fig. 14. The data are approximated by Eqs. (17) and (18)

$$b = B_1 k + B, \tag{28}$$

with

$$B = B_0 + b_1 \log \dot{\epsilon}. \tag{29}$$

Each set of data (corresponding to a fixed strain rate) is matched by Eq. (28) separately. The coefficients B_1 and B are calculated by the least-squares method. Although Fig. 14 reveals an acceptable agreement between the data and their fits by Eq. (28), some scatter of the data should be mentioned.

The coefficient B is plotted versus strain rate $\dot{\epsilon}$ in Fig. 15. The data are fitted by Eq. (29) with coefficients B_0 and b_1 determined by the least-squares technique. Fig. 15 demonstrates that Eq. (29) correctly approximates the experimental dependence $B(\dot{\epsilon})$.

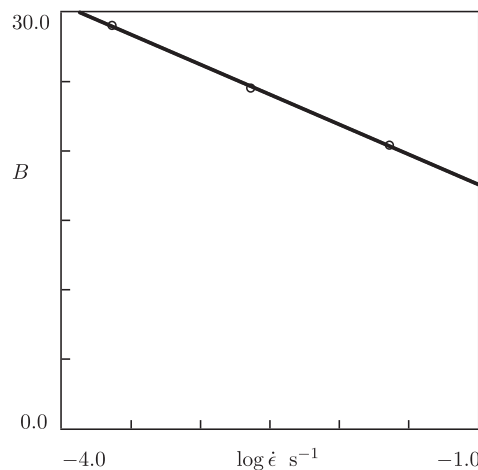The entire set of material constants in the stress–strain relations is reported in Table 1.

Fig. 15. Parameter B versus strain rate $\dot{\epsilon}$. Circles: treatment of observations. Solid line: approximation of the experimental data by Eq. (29).

Table 1
Adjustable parameters for PP/PE blends.

Parameter	Dimension	Value
E_0	GPa	0.12
E_1	GPa	1.34
a_1		1.13
b_1		−4.32
B_0		13.29
B_1		25.49
γ	s^{-1}	0.89
κ_0		0.42
κ_1		0.57
Σ_0		3.50
Σ_1		9.19

Figs. 1–3 show good agreement between the experimental data and the results of numerical simulation. Some discrepancies are to be mentioned for neat mPP at strains in the post-yield region of deformations. These discrepancies disappear when engineering stress σ is recalculated with account for volume changes induced by growth of voids (Fig. 5). We do not dwell on this issue, however, as the viscoelasto-plastic behavior of polymer blends is modeled in this study under the incompressibility hypothesis.

4.4. Creep test

To validate the constitutive equations, simulation is conducted of the time-dependent response of polymer blends in creep tests, and results of numerical analysis are compared with the observations reported in Figs. 7–9.

For a tensile creep test with a stress σ, the loading path of a creep curve is, first, modeled (uniaxial tension with strain rate $\dot{\epsilon} = 2.3 \cdot 10^{-2}$ s^{-1} until the instant when engineering stress equals σ). For this purpose, Eqs. (22), (25), and (26) are integrated numerically with the step $\Delta t = 5.0 \times 10^{-3}$ s. Afterwards, evolution of tensile strain with time is modeled by means of the following algorithm. The elastic strain is found from Eq. (25)

$$\epsilon_e(t) = \frac{\sigma}{E(1 - \phi(t))} + \kappa \int_0^\infty f(\nu) Z(t, \nu) \mathrm{d}\nu, \tag{30}$$

where $Z(t, \nu)$ is determined from Eq. (26). The macro-strain ϵ is calculated by integration of the differential equation

$$\frac{\mathrm{d}\epsilon}{\mathrm{d}t} = \left(1 - \phi - \frac{b\sigma}{E}\right)^{-1} \frac{\mathrm{d}\epsilon_e}{\mathrm{d}t}, \tag{31}$$

which follows from Eqs. (21) and (22). The function $\phi(t)$ is found from Eq. (22), and the coefficient b is given by Eqs. (28) and (29).

Results of numerical analysis are depicted in Figs. 7–9, which show excellent agreement between the experimental data and their predictions by the model. Small discrepancies are observed at large stresses only (Fig. 9) when transition occurs from secondary to tertiary creep flow.

5. Numerical simulation

The aim of numerical simulation is twofold: (i) to demonstrate that the model captures all stages of creep flow (including tertiary creep), and (ii) to assess the time-dependent response in long-term creep tests and to evaluate the stress–lifetime diagram under conditions of creep rupture.

5.1. Short-term creep tests

To show that the stress–strain relations adequately describe all stages of creep flow (Fig. 9 reveals some discrepancies between the observations and predictions of the model after transition to ter-
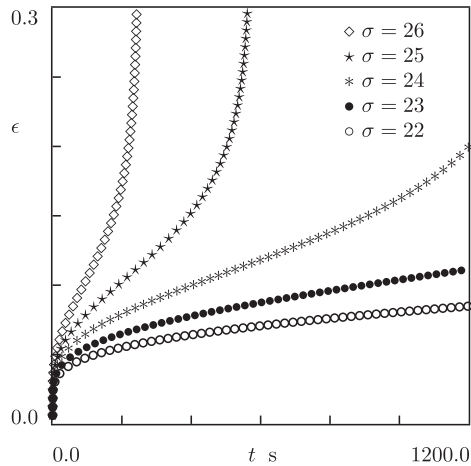
Fig. 16. Strain ϵ versus time t. Symbols: results of numerical simulation for short-term creep tests on mPP with various stresses σ MPa.

tiary creep), simulation is conducted of short-term tensile creep tests with stresses σ = 22, 23, 24, 25, and 26 MPa. Numerical analysis is performed for creep tests (with strain rate $\dot{\epsilon} = 2.3 \cdot 10^{-2}$ s^{-1} along the loading path) on mPP (k = 1). Results of simulation are presented in Fig. 16, where tensile strain ϵ is plotted versus time t. Fig. 16 demonstrates that strain ϵ monotonically increase with stress σ and transition to tertiary creep flow occurs in short-term tests with stresses exceeding 22 MPa.

5.2. Long-term creep tests

To evaluate lifetime of polymer blends under condition of creep rupture, simulation is conducted of long-term creep tests. Given a tensile stress σ, time-to-failure t_f is determined from the condition that strain $\epsilon(t_f)$ reaches its critical value ϵ_c = 0.3 (this value is taken from Fig. 16, which shows that the graphs $\epsilon(t)$ become practically vertical at $\epsilon = \epsilon_c$). Dependencies of σ on time-to-failure t_f are reported in Fig. 17 for blends with k = 0.2, 0.4, 0.6, 0.8, and 1.0. Each set of data is approximated by the Eyring equation

$$\sigma = S_0 - S_1 \log t_f, \tag{32}$$

where the coefficients S_0 and S_1 are found by the least-squares method. Fig. 17 demonstrates that Eq. (32) provides an acceptable approximation of the data.
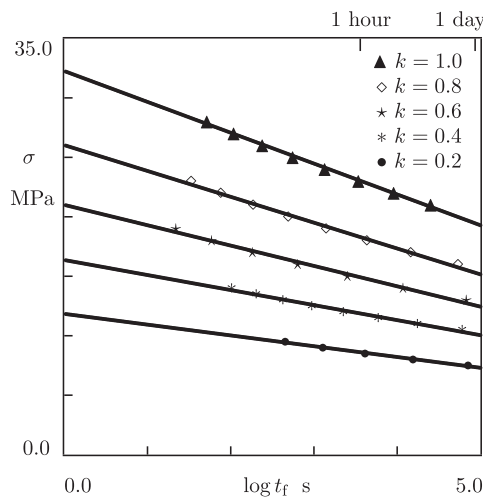

Fig. 17. Stress σ versus time-to-failure t_f. Symbols: results of numerical simulation for creep tests on blends with various concentrations k of mPP. Solid lines: their approximation by Eq. (32).
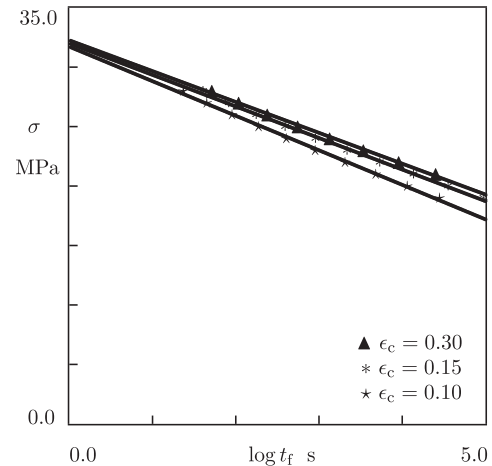

Fig. 18. Stress σ versus time-to-failure t_f. Symbols: results of numerical simulation for creep tests on mPP with various maximum strains ϵ_c. Solid lines: their approximation by Eq. (32).

As the constitutive model has been derived within the linear theory with small deformations, a question arises regarding applicability of this approach to the analysis of creep rupture with a relatively large maximum strain ϵ_c = 0.3. To assess the effect of maximum strain on stress-lifetime diagram, numerical analysis is conducted of long-term creep tests with various maximum strains ϵ_c. Results of simulation for mPP are reported in Fig. 18 together with their approximation by Eq. (32). This figure shows that the stress–lifetime diagrams with ϵ_c = 0.15 and 0.3 practically coincide, which implies that the effect of geometrical nonlinearity on time-to-failure is of secondary importance. The results of simulation with ϵ_c = 0.1 (according to Fig. 16, this strain is below the critical strain for transition to tertiary creep flow) differ noticeably from those with ϵ_c = 0.15 and 0.3. The latter means that an accurate assessment of critical strain for transition from secondary to tertiary creep plays a key role is evaluation of lifetime.

Klompen et al. (2005), van Erp et al. (2009), and Engels et al. (2010) have recently proposed an empirical relation between the dependence of yield stress on strain rate $\sigma_y(\dot{\epsilon})$ and the dependence of stress on time-to-failure $\sigma(t_f)$. Under the assumption that both functions are adequately described by Eqs. (1) and (32), it was postulated that the coefficients σ_{y1} and S_1 (that determine slopes of appropriate curves in semi-logarithmic coordinates) coincided. This statement was confirmed for PP in Drozdov and Christiansen (2009) by comparison of experimental data in tensile tests with results of numerical analysis for long-term creep tests.

To examine this assertion for PP/PE blends, σ_{y1} and S_1 are plotted versus mass fraction of mPP k in Fig. 19. The data are fitted by the linear equations

$$\sigma_{y1} = c_0 + c_1 k, \quad S_1 = C_0 + C_1 k, \tag{33}$$

where the coefficients are calculated by the least-squares technique. The following conclusions are drawn from Fig. 18: (i) the parameters σ_{y1} and S_1 linearly grow with mass fraction of mPP, (ii) for all compositions of blend, σ_{y1} exceeds S_1, which implies that slope of the curve $\sigma_y(\dot{\epsilon})$ underestimates lifetime t_f. The difference between S_1 and σ_{y1} is negligible (about 19%) for mPP (k = 1.0), but it becomes noticeable (by twice) for blends with low content of mPP (k = 0.4). Based on observations reported in Figs. 1–3, one can infer that σ_{y1} and S_1 coincide only when polymers reveal pronounced yield points on their stress–strain diagrams.
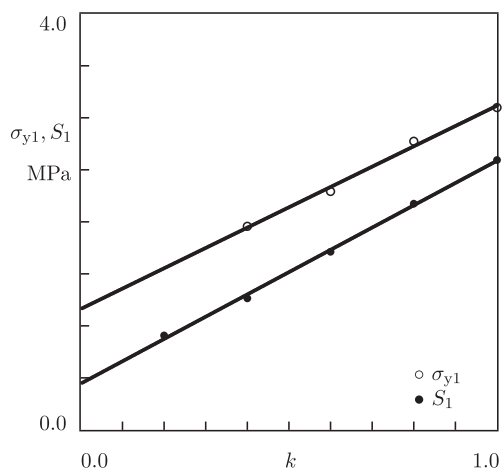
Fig. 19. Coefficients σ_{y1} and S_1 versus mass fraction of mPP k. Unfilled circles: treatment of observations in tensile tests. Filled circles: results of numerical simulation for creep tests. Solid lines: their approximation by Eq. (33).

6. Concluding remarks

Observations are reported in tensile tests with constant strain rates, relaxation tests, and creep tests on blends of low density polyethylene and metallocene catalysed polypropylene. The following features of the experimental investigation are to be mentioned: (i) a thorough analysis of the mechanical response is conducted on six blends with various mass fractions of mPP ranging from 0 to 100%, (ii) tests are performed with two extensometers that allow engineering stress, tensile strain, and transverse strain to measure simultaneously.

A constitutive model is developed for the viscoelastic and viscoplastic responses of binary blends at arbitrary three-dimensional deformations with small strains. The stress–strain relations are derived by using the Clausius–Duhem inequality. Given a blend's composition, they involve seven material constants with transparent physical meaning.

Adjustable parameters in the constitutive equations are determined by fitting the observations in tensile tests with constant strain rates and relaxation tests. These quantities change consistently with blend's composition following linear phenomenological relations similar to the rule of mixture. The model is validated by comparison of experimental data in creep tests with results of numerical simulation.

The stress–strain relations are applied for assessment of lifetime of polymer blends under condition of creep rupture. It is shown that (i) the Eyring equation correctly describes the effect of tensile stress on time-to-failure, and (ii) the empirical method grounded on the dependence of yield stress on strain rate underestimates time-to-failure.

In order to reduce the number of adjustable parameters in the stress–strain relations, several simplifying assumptions have been introduced. In particular, (i) analysis of the viscoelasto-plastic response of polymer blends is conducted within the concept of small deformations (whereas the maximum strain in tensile tests ϵ_{max} = 0.25 is not very small), (ii) the blends are treated as isotropic media (although some anisotropy of specimens is induced by the injection-molding process), and (iii) damage accumulation driven by nucleation and growth of micro-voids is disregarded (despite the fact that an increase in volume strain is observed in the post-yield region of deformations). A detailed analysis of these factors on the viscoelastic and viscoplastic responses of polymer blends will be the subject of a subsequent publication, where predictions of the constitutive model are compared with observations in three-points bending and indentation tests.

References

Bauwens-Crowet, C., Bauwens, J.-C., Homes, G., 1972. The temperature dependence of yield of polycarbonate in uniaxial compression and tensile tests. J. Mater. Sci. 7, 176–183.

Chen, X.-H., Mai, Y.-W., 1999. Three-dimensional elastoplastic finite element modelling of deformation and fracture behaviour of rubber-modified polycarbonates at different triaxiality. J. Mater. Sci. 34, 2139–2149.

Derrida, B., 1980. Random-energy model: limit of a family of disordered models. Phys. Rev. Lett. 45, 79–92.

Drozdov, A.D., Christiansen, J.deC., 2007. Cyclic deformation of ternary nanocomposites: experiments and modeling. Int. J. Solids Struct. 44, 2677–2694.

Drozdov, A.D., Christiansen, J.deC., 2008. Thermo-viscoelastic and viscoplastic behavior of high-density polyethylene. Int. J. Solids Struct. 45, 4274–4288.

Drozdov, A.D., Christiansen, J.deC., 2009. Creep failure of polypropylene: experiments and constitutive modeling. Int. J. Fracture 159, 63–79.

Engels, T.A.P., Sontjens, S.H.M., Smit, T.H., Govaert, L.E., 2010. Time-dependent failure of amorphous polylactides in static loading conditions. J. Mater. Sci. Mater. Med. 21, 89–97.

Hiss, R., Hobeika, S., Lynn, C., Strobl, G., 1999. Network stretching, slip processes, and fragmentation of crystallites during uniaxial drawing of polyethylene and related copolymers. A comparative study. Macromolecules 32, 4390–4403.

Jose, S., Aprem, A.S., Francis, B., Chandy, M.C., Werner, P., Alstaedt, V., Thomas, S., 2004. Phase morphology, crystallisation behaviour and mechanical properties of isotactic polypropylene/high density polyethylene blends. Eur. Polym. J. 40, 2105–2115.

Klompen, E.T.J., Engels, T.A.P., van Breemen, L.C.A., Schreurs, P.J.G., Govaert, L.E., Meijer, H.E.H., 2005. Quantitative prediction of long-term failure of polycarbonate. Macromolecules 38, 7009–7017.

Kuroda, M., Handa, Y., Ishikawa, M., 2004. Modelling of overall plastic deformation in rubber-toughened polymers. Acta Mech. 172, 95–112.

Liang, J.Z., Li, R.K.Y., 2000. Rubber toughening in polypropylene: a review. J. Appl. Polym. Sci. 77, 409–417.

Li, J., Shanks, R.A., Long, Y., 2003. Miscibility and crystallization of metallocene polyethylene blends with polypropylene. J. Appl. Polym. Sci. 87, 1179–1189.

Machado, G., Kinast, E.J., Scholten, J.D., Thompson, A., Vargas, T.D., Teixeira, S.R., Samios, D., 2009. Morphological and crystalline studies of isotactic polypropylene plastically deformed and evaluated by small-angle X-ray scattering, scanning electron microscopy and X-ray diffraction. Eur. Polym. J. 45, 700–713.

Machmud, M.N., Omiya, M., Inoue, H., Kishimoto, K., 2006. A phenomenological constitutive model constructed for PC/ABS blends. Key Eng. Mater. 306–308 (II), 989–994.

Mae, H., Omiya, M., Kishimoto, K., 2008. Material ductility and toughening mechanism of polypropylene blended with styrene–butadiene–styrene triblock copolymer at high strain rate. J. Appl. Polym. Sci. 110, 3941–3953.

Mathew, M.T., Novo, J., Rocha, L.A., Covas, J.A., Gomes, J.R., 2010. Tribological, rheological and mechanical characterization of polymer blends for ropes and nets. Tribology Int. 43, 1400–1409.

Na, B., Wang, K., Zhang, Q., Du, R., Fu, Q., 2005. Tensile properties in the oriented blends of high-density polyethylene and isotactic polypropylene obtained by dynamic packing injection molding. Polymer 46, 3190–3198.

Ono, K., Ogita, H., Okamoto, K., Yamaguchi, M., 2009. Processability and mechanical properties for binary blends of PP and LLDPE produced by metallocene catalyst. J. Appl. Polym. Sci. 113, 3368–3375.

Razavi-Nouri, M., 2007. Properties of polypropylene and metallocene-prepared polyethylene blends: crystallization behavior and interaction parameter. Polym. Testing 26, 108–115.

Shaoqiu, S., Bing, Y., Lili, W., 2007. The thermoviscoelastic constitutive equation of PP and PA blends and its rate-temperature equivalency at high strain rates. Macromol. Symp. 247, 28–34.

Steenbrink, A.C., van der Giessen, E., 1997. Void growth in glassy polymers: effect of yield properties on hydrostatic expansion. Int. J. Damage Mech. 6, 317–330.

Tanaka, F., Edwards, S.F., 1992. Viscoelastic properties of physically cross-linked networks. Transient network theory. Macromolecules 25, 1516–1523.

van Erp, T.B., Reynolds, C.T., Peijs, T., van Dommelen, J.A.W., Govaert, L.E., 2009. Prediction of yield and long-term failure of oriented polypropylene: kinetics and anisotropy. J. Polym. Sci. B: Polym. Phys. 47, 2026–2035.

Xie, M., Chen, J., Li, H., 2009. Morphology and mechanical properties of injection-molded ultrahigh molecular weight polyethylene/polypropylene blends and comparison with compression molding. J. Appl. Polym. Sci. 111, 890–898.

Zahran, R.R., El-Latif, M.M.A., Konsowa, A.E.-A., Awwad, M., 2010. Development of isotropic compatible HDPE/PP blends for structural applications. J. Appl. Polym. Sci. 115, 1407–1418.